# Aerosol Jet Printing of the Ultramicroporous Calcium Squarate Metal Organic Framework

Dmitry E. Kravchenko†, Aleksander Matavž†, Víctor Rubio-Giménez†, Hanne Vanduffel†, Margot Verstreken†, and Rob Ameloot*†

† Department of Microbial and Molecular Systems, Centre for Membrane Separation, Adsorption, Catalysis and Spectroscopy, KU Leuven - Celestijnenlaan 200F, 3001 Leuven, Belgium

**ABSTRACT:** Efficient methods to deposit thin layers of metal-organics frameworks (MOFs) are needed to integrate these microporous materials into microelectronics, sensing devices, and membranes. Herein, we report for the first time the direct aerosol jet printing of a MOF material. The ultramicroporous MOF [$Ca(C_4O_4)(H_2O)$] (UTSA-280) was deposited from an aqueous precursor solution. In addition to blanket coatings, aerosol jet printing provides direct access to patterned coatings with a resolution of 100 µm via a digital, maskless approach. Moreover, by enabling spatial control over the layer thickness via the number of passes of the nozzle, this direct-write approach presents a more accessible alternative to advanced patterning techniques such as grayscale lithography.

Metal-organic frameworks (MOFs) are microporous crystalline coordination polymers with unique adsorption properties. They have shown tremendous potential in catalysis,[1] gas storage,[2] separation,[3] and microelectronics.[4] As sensor coatings, they can concentrate the analyte on the sensor surface, in some cases selectively.[5,6] However, their integration is hindered by the lack of facile and versatile deposition and patterning techniques.[7,8] Solution-based techniques for MOF deposition, such as chemical solution growth or liquid-phase epitaxy, could cause corrosion or contamination.[4] Chemical vapor deposition circumvents these risks,[9] but is limited by the reactivity of the metal precursor and the volatility of the linker. A plethora of patterning methods have been demonstrated for MOF coatings. Subtractive approaches such as lift-off patterning[9,10] or resist-free direct lithography[11] involve modifying the whole substrate, increasing the risk of contamination by residues. In contrast, additive patterning techniques, such as selective growth,[12] microcontact,[12,13] and inkjet printing[14,15] deposit the target material only on a confined area of the substrate. Inkjet printing is particularly attractive thanks to its low cost, non-contact and mask-free nature, digital control, and scalability.[16] However, it requires careful ink formulation within a narrow window of viscosity and surface tension.

Aerosol jet printing (AJP) is an emerging contactless direct-write technique based on a focused aerosol stream. While it shares most of the advantages of inkjet printing,[17] the viscosity of the atomized liquid does not play an important role, and no ink optimization is needed. Unlike other patterning techniques, it can be used to directly produce a freeform pattern on virtually any type of substrate, including 3D objects. Typically, AJP is used to print electronic components consisting of inorganic materials, such as conductive silver lines,[18] graphene interconnects,[19] and perovskite X-ray photodetectors.[20] The resolution mainly depends on the jet shape and can reach down to 50 µm when efficient aerodynamic focusing is applied.[21]

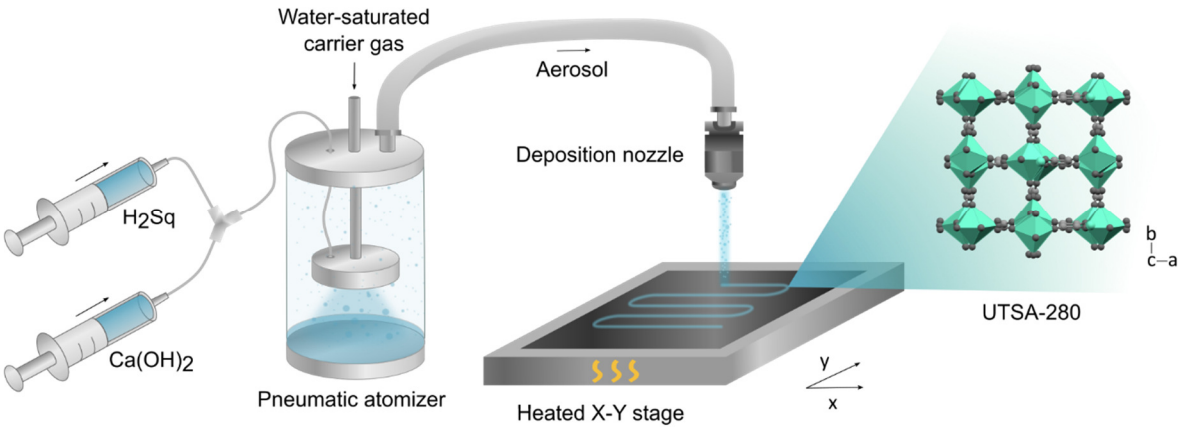


**Figure 1**. Schematic representation of the aerosol jet printing set-up used to deposit UTSA-280. [$CaO_6$] polyhedra are shown in green, C and O atoms are shown in grey.

To the best of our knowledge, AJP has not been employed to deposit any MOF before. However, the feasibility of AJP of MOFs is hinted at by the previously reported spray deposition of blanket coatings of MOFs. Submicron coatings of terbium terephthalate were grown on heated substrates by atomizing the metal salt and linker solution separately and directing both aerosols simultaneously to the substrate.[22] In addition, precursors have been sprayed on a substrate sequentially, with a washing step in-between, as demonstrated in the liquid-phase epitaxy growth of HKUST-1.[23,24] Further, preformed MOF particles have been deposited through supersonic cold spraying[25] and spray-drying of synthesis solutions is an established technique to synthesize various MOFs in powder form.[26,27] Based on these reports, we expected that two requirements must be met to deposit a MOF coating from a precursor solution through AJP: (1) the solution must remain clear, without precipitation, and (2) ideally only volatile by-products form that can later be easily removed by mild heating.

To demonstrate AJP of MOFs, we targeted calcium squarate [$Ca(C_4O_4)(H_2O)$] (UTSA-280) because it can be synthesized from an aqueous solution in a manner satisfying both criteria indicated above. Moreover, the use of water as a solvent avoids the risk associated with flammable aerosols. As a rigid ultramicroporous MOF (*i.e.*, with pores smaller than 7 Å),[28] UTSA-280 discriminates between small molecules of similar sizes. For instance, it selectively adsorbs ethylene over ethane, even though both differ by only 0.28 Å in kinetic diameter.[29] In a typical synthesis, a saturated aqueous solution of sodium squarate ($Na_2Sq$) is mixed with an aqueous solution of calcium nitrate, resulting in immediate precipitation of 100-500 µm needles.[29] Recently, a room-temperature mechanochemical synthesis of UTSA-280 was reported that uses CaO or $Ca(OH)_2$ and squaric acid ($H_2Sq$) as precursors and generates water as the only by-product. [30] We observed that mixing a 10 mM aqueous solution of $Ca(OH)_2$ and $H_2Sq$ results in a solution that does not produce a visible precipitate for at least several hours (**Fig. S1**). This solution does, however, produce UTSA-280 crystals upon evaporation. Evaporation-induced MOF growth has previously been used for patterned deposition of HKUST-1,[13,31] including through inkjet printing.[32]

The setup used for AJP of UTSA-280 is shown in **Figure 1.** Schematic representation of the aerosol jet printing set-up used to deposit UTSA-280. [CaO6] polyhedra are shown in green, C and O atoms are shown in grey.. Two syringes with $Ca(OH)_2$ and $H_2Sq$ solutions are placed in a syringe pump. After mixing in a 3-way valve, the precursor solution is fed into a pneumatic atomizer containing a laser-cut ruby orifice. The pressurized carrier gas jet passes through the orifice at high velocity and breaks the liquid into micrometer-sized droplets. If a dry carrier gas is used, water evaporation from the droplets causes the undesired formation of an aerosol of UTSA-280 particles, which bounce off the substrate instead of sticking to it. To avoid this effect, the carrier gas was saturated with water vapor before introducing it into the atomizer. When hitting the bottom of the atomizer reservoir, larger droplets coalesce, and smaller ones bounce off. The fine aerosol is carried by the gas stream to the deposition head. Finally, as the droplets pass through the deposition nozzle, they are accelerated towards the substrate in an impinging jet. The deposition spot depends on the jet shape and velocity, as well as the droplet size distribution. While larger (roughly >3 µm) droplets deposit in a spot smaller than the nozzle orifice, smaller (roughly <2 µm) droplets hit the surface further away from the jet centerline (overspray).[33] A fraction of the submicron-sized droplets are unable to impact the substrate and is carried away by the deflecting gas flow, reducing the deposition efficiency. To deposit on a larger area, the deposition nozzle was fixed on a PRUSA i3 MK3 printhead. The movement of the printhead and printbed in the X and Y direction respectively was programmed by GCode commands. To optimize the deposition process, the following key parameters were varied: substrate temperature, precursor concentration, and number of passes .The substrate temperature directly affects convection flow, solvent evaporation rate, surface tension of the droplets on the surface, and MOF crystallization. Consequently, the deposition thickness, resolution, and crystal morphology will vary substantially for different substrate temperatures. To study these effects, rectangular areas (3x4 $mm^2$) were printed by moving the nozzle in a zig-zag pattern (**Fig. S2a**) on silicon substrates at 30, 60, and 90 °C. As seen in **Fig. 2a**, the coverage of the coating decreases drastically with increasing temperature. This deterioration can be attributed to faster drying of the aerosol droplets before they reach the substrate. Smaller solid particles bounce off the surface, decreasing the deposition efficiency

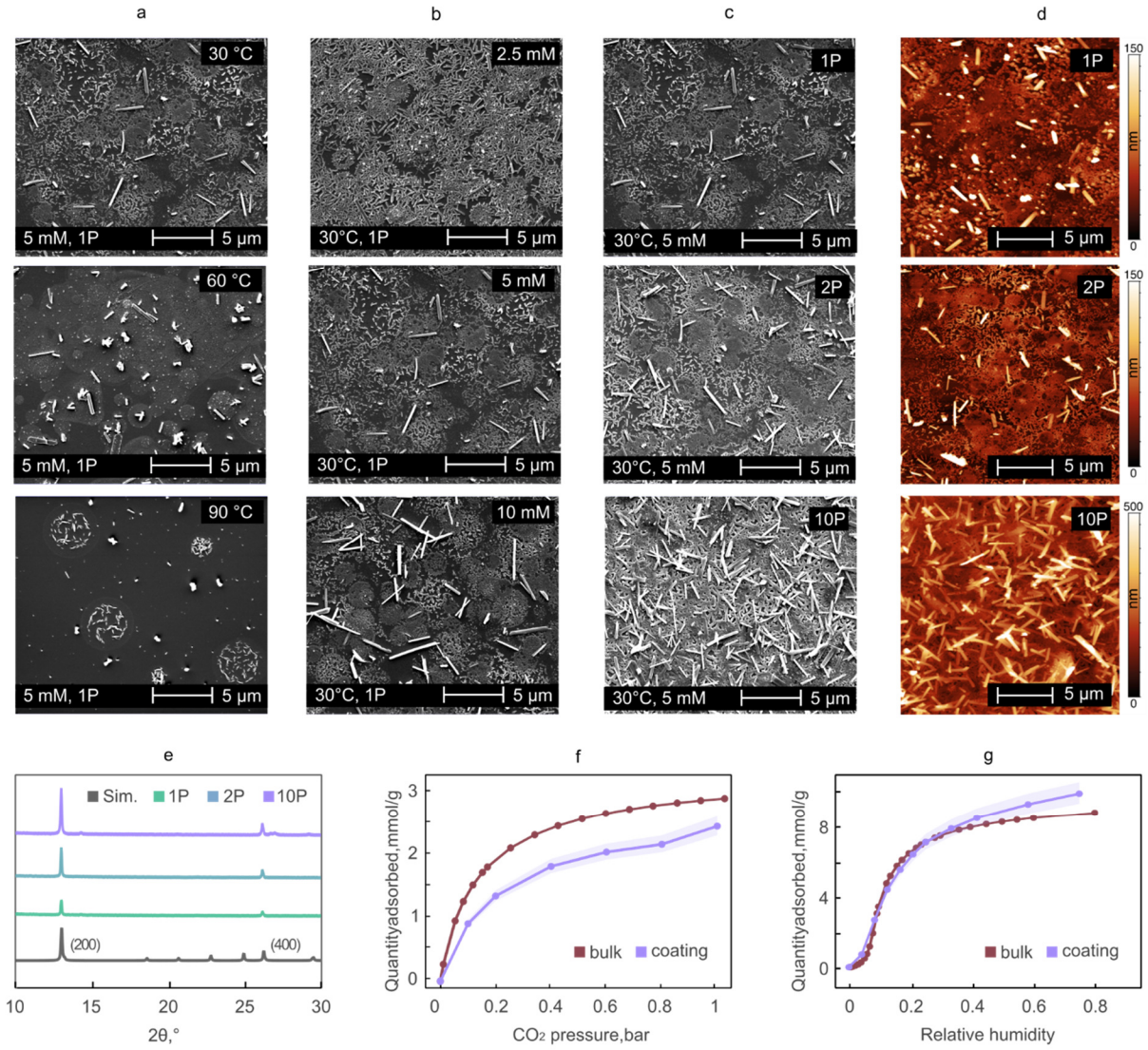


**Figure 2**. Characterization of UTSA-280 coatings deposited via AJP. SEM micrographs of coatings deposited (a) on silicon substrates kept at 30, 60, and 90 °C (1 pass, 5 mM precursor solutions), (b) from 2.5, 5, and 10 mM $Ca(OH)_2$ and $H_2Sq$ precursor solutions (1 pass, substrate at 30 °C), and (c) in 1, 2, and 10 passes (5 mM precursor solutions, substrate at 30 °C). (d) AFM images of UTSA-280 deposited in 1, 2, and 10 passes (5 mM precursor solutions, substrate at 30 °C). (e) GIXRD of UTSA-280 films deposited in 1, 2, and 10 passes along with the simulated diffractograms. (f) $CO_2$ and (g) $H_2O$ physisorption isotherms at 20 °C on bulk UTSA-280 powder and a QCM sensor coated via AJP. The shaded area represents the 95% confidence interval based on the uncertainty in the mass determination of the MOF layer.

and surface coverage. At 30 °C, this effect is negligible, and the highest deposition rate is observed. The different morphology of MOF particles deposited at 90 °C and the absence of the round marks left by drying droplets around some of the larger particles suggests that they were formed already in the aerosol phase, before hitting the substrate. Considering both deposition efficiency and coverage, 30 °C was selected as the optimal substrate temperature.

The precursor concentration also affects the deposition thickness, coverage, and morphology. The upper concentration limit is dictated by the onset of crystallization upon mixing the metal and linker precursor solutions, as premature crystallization may clog the nozzle orifice. We set the upper concentration limit of both precursors at 10 mM, as mixing these concentrations does not produce any visible precipitate for at least 5 h (**Fig.** S1). While there is no lower limit, the increasing printing time needed to deposit a film of a given thickness makes very dilute solutions impractical to work with. To investigate the impact of precursor concentration on the film quality, we printed rectangular areas of UTSA-280 (3x4 $mm^2$) in a single pass using 2.5, 5, and10 mM solutions of $Ca(OH)_2$ and $H_2Sq$. The print speed was set at 200, 400, and 800 mm/min, respectively, to keep the deposited MOF per unit area roughly constant. As seen in **Fig.**

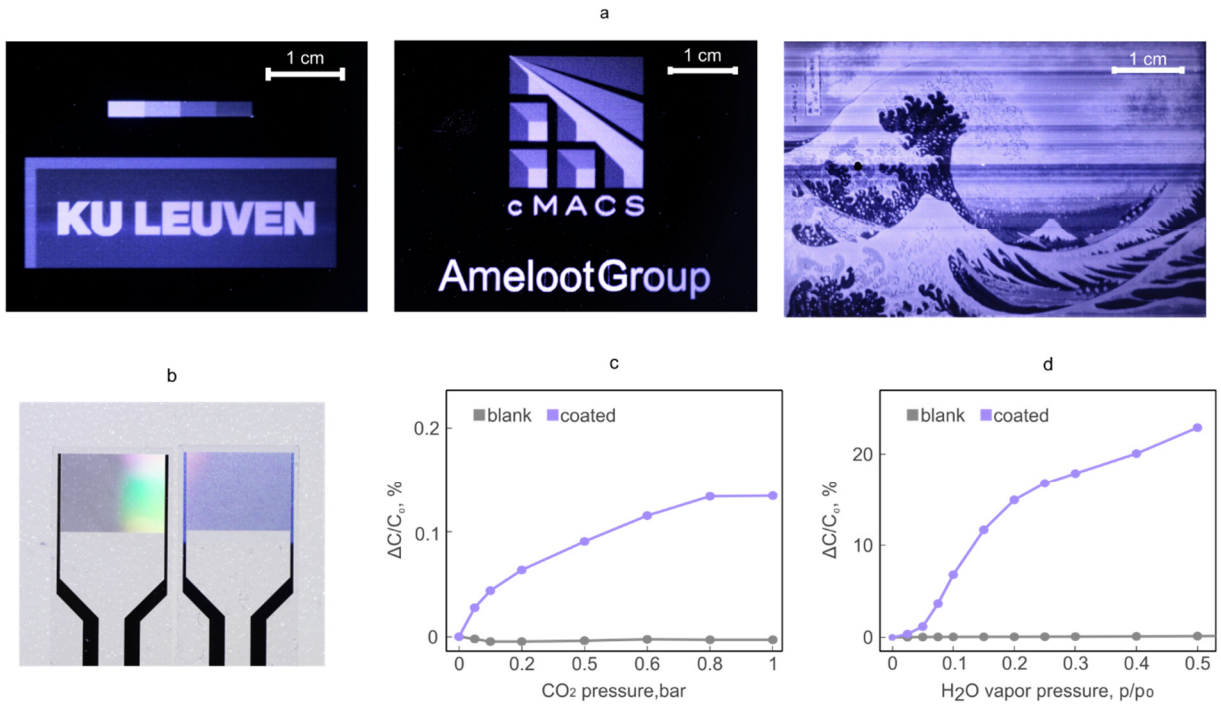


**Figure 3**. (a) Optical photographs of images printed with an UTSA-280 aerosol jet, including a reproduction of the "Great Wave off Kanagawa" by Hokusai. The images contain five shades of grey corresponding to 0, 1, 2, 5, and 10 print passes. (b) Optical photograph of an uncoated (left) and an UTSA-280-coated IDE capacitive sensor (right). Response curve of the UTSA-280-coated IDE capacitive sensor to (c) $CO_2$ and (d) $H_2O$ at 100 kHz. The response is expressed as $\Delta C/C_0$, where $C_0 = 98.3$ pF is the capacitance of the sensor in the absence of an analyte.

**2b**, higher precursor concentrations lead to a decrease of coverage accompanied by an increase in the crystallite size. The sample deposited from the 10 mM solutions shows needles reaching several microns in length on top of smaller crystallites. For 2.5 and 5 mM precursors, more of the smaller crystallites are formed, although large needles appear as well when printing the same area multiple times (**Fig. S3**). Considering the trade-off between better surface coverage and printing speed, we chose 5 mM as the optimal precursor concentration.

For the selected substrate temperature and precursor concentration, we considered the following strategies to improve the coverage: (1) increasing the liquid flow rate, (2) decreasing the linear speed of the nozzle, and (3) printing in multiple passes. The former led to accelerated aerosol coalescence on tube walls causing the nozzle to sputter. Decreasing the print speed below a certain point led to excessive fluid and spreading on the surface. Nevertheless, additional passes of the nozzle result in improved coverage (**Fig. 2c, d**). However, the surface is not entirely covered even after 10 passes (**Fig. S4**). We speculate that because the initially formed MOF layer is less hydrophilic than the bare substrate, the aerosol droplets deposited on top do not wet the surface and thus start growing a second layer before sealing the first one. That second layer consists of loosely packed 1-5 µm long needles. These observations are confirmed by AFM topography images (**Fig 2f**) and the sharp increase of the root mean square (RMS) roughness from 31 nm for 1 pass to 87 nm for 10 passes. In all cases, the crystallinity of the UTSA-280 was confirmed by X-ray diffraction (XRD, **Fig 2e**). As expected, the intensities of the peaks roughly scale with the number of passes, indicating progressively thicker crystalline coatings. Only the Bragg peaks corresponding to (h00) planes are visible, indicating that the crystallites have a preferential (100) out-of-plane orientation. Therefore, the 1D UTSA-280 pores are laying parallel to the substrate (**Fig 1**). To showcase the versatility of AJP for deposition of MOFs, we applied the same conditions to deposit ZIF-8 from $[Zn(NH_3)_4](OH)_2$ and 2-methylimidazole. The formation of ZIF-8 was confirmed by XRD (**Fig. S13**).

To assess the deposition efficiency and the adsorption behavior of UTSA-280 deposited via AJP, a layer was grown in 10 passes on a $SiO_2$-coated quartz crystal microbalance (QCM) sensor. Mass determination of QCM coatings can require sophisticated modeling based on the resonant frequencies ($f_n$) and bandwidths ($\Gamma_n$) for different overtones ($n$). However, in the specific case of a rigid coating, the energy dissipation in the film is low and the resonant frequency shift ($\Delta f_n$) of a QCM sensor is linearly proportional to the mass change according to the Sauerbrey equation.[34] Whether or not a coating can be considered rigid can be assessed by comparing $f_n$ and $\Gamma_n$ before and after deposition. If the resonance bandwidth shift ($\Delta\Gamma_n$), which is proportional to the energy dissipation increase, is much smaller than $\Delta f$, the coating can be considered rigid.[35] Typically, the Sauerbrey equation is not valid when the coating consists of loosely packed particles with poor adhesion to the surface.[34] However, the deposited MOF coating can be regarded as rigid as the ratio $\Delta\Gamma_n/\Delta f_n$ is < 0.1 for all measured overtones (**Fig. S6**). The mass of the MOF layer calculated from the Sauerbrey equation was found to be only 0.8% of the theoretically expected mass based on the precursor consumption. As we measured the atomization efficiency to be 10%, based on the difference between the liquid volume injected and accumulated in the atomizer, the deposition efficiency (*i.e.*, the sticking coefficient) was about 8%.

The coated sensor was activated inside the QCM measurement cell overnight at 100 °C under a nitrogen flow to remove excess linker and physisorbed water. A $CO_2$ adsorption isotherm was measured by exposing the sensor to different concentrations of $CO_2$ diluted in $N_2$ (**Fig. 2f**). In comparison with bulk UTSA-280, the uptake on the QCM is only slightly lower across the measured pressure range. Both isotherms have the characteristic shape of micropore filling (IUPAC type I).[36] Similarly, a water adsorption isotherm was measured on the same sensor (**Fig. 2g**). At low vapor pressures ($p/p^0 < 0.2$), the isotherm measured for the coating overlaps with the one obtained through volumetric measurements on UTSA-280 powder, both displaying the type I shape.[36] In comparison to the powder, the coating consists of smaller crystallites with a higher external surface area. As a result, the specific water uptake is higher for the coating at higher vapor pressures. To demonstrate the stability of the coating, we stored the sensor for 6 weeks in ambient air and repeated the water adsorption experiment (**Fig. S7**). The minimal reduction in adsorption capacity confirms UTSA-280 as an attractive sensing material.

To assess the printing resolution, we deposited a series of parallel lines with the interline distance varying from 25 to 250 µm. Although overspray causes line broadening (**Fig. S8**), the lines are still discernable for a 150 µm pitch, which we define as the resolution (*i.e.*, the minimum interline distance at which individual lines can still be resolved). Interestingly, the addition of 0.5 wt% hexanol brings the resolution down to 100 µm. To elucidate this effect, we measured the contact angle of the precursor solution on the substrate, which drops from 24 to 15° upon the addition of hexanol (**Fig. S9**). A droplet with a lower contact angle is less susceptible to movement by the impinging jet[37] and dries faster because of its higher surface area. Furthermore, the addition of hexanol does not adversely affect the crystallinity or the porosity of the deposited coatings (**Fig. S10**). Therefore, it was adopted as part of the standard printing protocol for patterned MOF layers. The resolution can likely be further improved by using a nozzle with aerodynamic focusing.[38]

As demonstrated above, the thickness of the deposited layer can be controlled via the number of passes of the nozzle. This capability enables AJP to spatially control the layer thickness within the same coating, making the method an alternative to grayscale lithography.[39] To demonstrate this ability, three images containing five shades of gray were printed. The greyscale levels were translated into different thicknesses by printing 0, 1, 2, 5, and 10 passes (**Fig. 3a**). Even though UTSA-280 itself is colorless, areas with a different coating thickness are visually distinct, with thicker layers scattering more light. The horizontal stripes in the reproduction of the "Great Wave off Kanagawa" are an artifact caused by partial clogging of the atomizer. Such clogging issues could be avoided by switching to an ultrasonic atomizer.[22,24,25]

To showcase AJP as a facile direct-write, resist-free patterning technique, we fabricated a capacitive sensor in a single deposition step. A UTSA-280 coating (10 passes) was deposited on top of a set of platinum interdigitated electrodes (IDE) with a 5 µm finger width and spacing (**Fig 3b and S11**). The sensor was activated as for the QCM substrates and subsequently exposed to different concentrations of $CO_2$ and $H_2O$ while monitoring the capacitance (**Fig 3c, d**). As the adsorbate molecules fill the pores and adsorb on the outer surface of the MOF, the dielectric constant of the layer increases. The much higher sensitivity to water arises from its higher dielectric constant (80 versus 1.5 for liquid $CO_2$ at 20°C)[40]. Both response curves follow the shape of the corresponding adsorption isotherms.

In conclusion, we demonstrated for the first time AJP of MOFs, with UTSA-280 as a showcase. In contrast to AJP of other materials, in this process, the MOF is formed on the substrate from drying precursor droplets. The coatings are crystalline and porous as-deposited, as proven by XRD and QCM adsorption experiments. Additionally, we explored the potential of AJP as a direct-write patterning technique by depositing complex patterns of UTSA-280 with variable thicknesses. Furthermore, we showed that AJP offers a facile route for fabricating MOF-based sensors by depositing a layer of UTSA-280 on an IDE capacitive sensor and testing it with two analytes. The versatility of the method was proven by deposition of ZIF-8 under similar conditions. These results illustrate the potential of AJP as a facile deposition method to integrate MOFs in various applications.

## ASSOCIATED CONTENT

### Supporting Information

Materials and methods, additional SEM images, and QCM data are free of charge via the Internet at http://pubs.acs.org

## AUTHOR INFORMATION

### Corresponding Author

Rob Ameloot – rob.ameloot@kuleuven.be

## ACKNOWLEDGMENT

This project has received funding from the European Union's Horizon 2020 research and innovation program under the FETOPEN-1-2016-2017 grant agreement No 801464 (project acronym: SPRINT), and from the European Research Council (ERC) under grant agreement No 716472 (acronym: VAPORE). We thank the Research Foundation Flanders (FWO Vlaanderen) for research projects G083016N, G0E6319N, G087422N, and for SB-PhD fellowships, as well as KU Leuven for research projects C32/18/056 and C14/20/085. D.E.K. acknowledges the Marie Sklodowska Curie Training Network HYCOAT, Grant Agreement 765378, for the financial support. V.R.-G. acknowledges FWO for a Marie Skłodowska Curie Actions—Seal of Excellence and a Junior Postdoctoral Fellowships (12Z6520N and 1263622N, respectively). H.V. and M.V. acknowledge FWO (1SB8519N and 1S48221N, respectively) for the financial support. We thank Miriam Candelaria Rodríguez González for her assistance in using the AFM. We thank Nathalie Wauteraerts for the GIXRD measurements.

## REFERENCES

(1) Yang, D.; Gates, B. C. Catalysis by Metal Organic Frameworks: Perspective and Suggestions for Future Research. *ACS Catal.* **2019**, *9* (3), 1779–1798. https://doi.org/10.1021/acscatal.8b04515.

(2) Ma, S.; Zhou, H.-C. Gas Storage in Porous Metal–Organic Frameworks for Clean Energy Applications. *Chem Commun* **2010**, *46* (1), 44–53. https://doi.org/10.1039/B916295J.

(3) Kwon, H. T.; Jeong, H.-K.; Lee, A. S.; An, H. S.; Lee, J. S. Heteroepitaxially Grown Zeolitic Imidazolate Framework Membranes with Unprecedented Propylene/Propane Separation Performances. *J. Am. Chem. Soc.* **2015**, *137* (38), 12304–12311. https://doi.org/10.1021/jacs.5b06730.

(4) Stassen, I.; Burtch, N.; Talin, A.; Falcaro, P.; Allendorf, M.; Ameloot, R. An Updated Roadmap for the Integration of Metal–Organic Frameworks with Electronic Devices and Chemical Sensors. *Chem. Soc. Rev.* **2017**, *46* (11), 3185–3241. https://doi.org/10.1039/C7CS00122C.

(5) Stassen, I.; Bueken, B.; Reinsch, H.; Oudenhoven, J. F. M.; Wouters, D.; Hajek, J.; Van Speybroeck, V.; Stock, N.; Vereecken, P. M.; Van Schaijk, R.; De Vos, D.; Ameloot, R. Towards Metal–Organic Framework Based Field Effect Chemical Sensors: UiO-66-$NH_2$ for Nerve Agent Detection. *Chem. Sci.* **2016**, *7* (9), 5827–5832. https://doi.org/10.1039/C6SC00987E.

(6) Wang, H.; Lustig, W. P.; Li, J. Sensing and Capture of Toxic and Hazardous Gases and Vapors by Metal–Organic Frameworks. *Chem. Soc. Rev.* **2018**, *47* (13), 4729–4756. https://doi.org/10.1039/C7CS00885F.

(7) Crivello, C.; Sevim, S.; Graniel, O.; Franco, C.; Pané, S.; Puigmartí-Luis, J.; Muñoz-Rojas, D. Advanced Technologies for the Fabrication of MOF Thin Films. *Mater. Horiz.* **2021**, *8* (1), 168–178. https://doi.org/10.1039/D0MH00898B.

(8) Ruiz-Zambrana, C. L.; Malankowska, M.; Coronas, J. Metal Organic Framework Top-down and Bottom-up Patterning Techniques. *Dalton Trans.* **2020**, *49* (43), 15139–15148. https://doi.org/10.1039/D0DT02207A.

(9) Stassen, I.; Styles, M.; Grenci, G.; Gorp, H. V.; Vanderlinden, W.; Feyter, S. D.; Falcaro, P.; Vos, D. D.; Vereecken, P.; Ameloot, R. Chemical Vapour Deposition of Zeolitic Imidazolate Framework Thin Films. *Nat. Mater.* **2016**, *15* (3), 304–310. https://doi.org/10.1038/nmat4509.

(10) Zhang, Z.; Zhao, Y.; Zhao, Z.; Huang, G.; Mei, Y. Atomic Layer Deposition-Derived Nanomaterials: Oxides, Transition Metal Dichalcogenides, and Metal–Organic Frameworks. *Chem. Mater.* **2020**, *32* (21), 9056–9077. https://doi.org/10.1021/acs.chemmater.9b04414.

(11) Tu, M.; Xia, B.; Kravchenko, D. E.; Tietze, M. L.; Cruz, A. J.; Stassen, I.; Hauffman, T.; Teyssandier, J.; De Feyter, S.; Wang, Z.; Fischer, R. A.; Marmiroli, B.; Amenitsch, H.; Torvisco, A.; Velásquez-Hernández, M. de J.; Falcaro, P.; Ameloot, R. Direct X-Ray and Electron-Beam Lithography of Halogenated Zeolitic Imidazolate Frameworks. *Nat. Mater.* **2021**, *20* (1), 93–99. https://doi.org/10.1038/s41563-020-00827-x.

(12) Lu, G.; Farha, O. K.; Zhang, W.; Huo, F.; Hupp, J. T. Engineering ZIF-8 Thin Films for Hybrid MOF-Based Devices. *Adv. Mater.* **2012**, *24* (29), 3970–3974. https://doi.org/10.1002/adma.201202116.

(13) Ameloot, R.; Gobechiya, E.; Uji-i, H.; Martens, J. A.; Hofkens, J.; Alaerts, L.; Sels, B. F.; De Vos, D. E. Direct Patterning of Oriented Metal-Organic Framework Crystals via Control over Crystallization Kinetics in Clear Precursor Solutions. *Adv. Mater.* **2010**, *22* (24), 2685–2688. https://doi.org/10.1002/adma.200903867.

(14) Su, C.-H.; Kung, C.-W.; Chang, T.-H.; Lu, H.-C.; Ho, K.-C.; Liao, Y.-C. Inkjet-Printed Porphyrinic Metal–Organic Framework Thin Films for Electrocatalysis. *J. Mater. Chem. A* **2016**, *4* (28), 11094–11102. https://doi.org/10.1039/C6TA03547G.

(15) da Luz, L. L.; Milani, R.; Felix, J. F.; Ribeiro, I. R. B.; Talhavini, M.; Neto, B. A. D.; Chojnacki, J.; Rodrigues, M. O.; Júnior, S. A. Inkjet Printing of Lanthanide–Organic Frameworks for Anti-Counterfeiting Applications. *ACS Appl. Mater. Interfaces* **2015**, *7* (49), 27115–27123. https://doi.org/10.1021/acsami.5b06301.

(16) Goel, P.; Singh, S.; Kaur, H.; Mishra, S.; Deep, A. Low-Cost Inkjet Printing of Metal–Organic Frameworks Patterns on Different Substrates and Their Applications in Ammonia Sensing. *Sens. Actuators B Chem.* **2021**, *329*, 129157. https://doi.org/10.1016/j.snb.2020.129157.

(17) Wilkinson, N. J.; Smith, M. A. A.; Kay, R. W.; Harris, R. A. A Review of Aerosol Jet Printing—a Non-Traditional Hybrid Process for Micro-Manufacturing. *Int. J. Adv. Manuf. Technol.* **2019**, *105* (11), 4599–4619. https://doi.org/10.1007/s00170-019-03438-2.

(18) Mahajan, A.; Frisbie, C. D.; Francis, L. F. Optimization of Aerosol Jet Printing for High-Resolution, High-Aspect Ratio Silver Lines. *ACS Appl. Mater. Interfaces* **2013**, *5* (11), 4856–4864. https://doi.org/10.1021/am400606y.

(19) Jabari, E.; Toyserkani, E. Micro-Scale Aerosol-Jet Printing of Graphene Interconnects. *Carbon* **2015**, *91*, 321–329. https://doi.org/10.1016/j.carbon.2015.04.094.

(20) Glushkova, A.; Andričević, P.; Smajda, R.; Náfrádi, B.; Kollár, M.; Djokić, V.; Arakcheeva, A.; Forró, L.; Pugin, R.; Horváth, E. Ultrasensitive 3D Aerosol-Jet-Printed Perovskite X-Ray Photodetector. *ACS Nano* **2021**, *15* (3), 4077–4084. https://doi.org/10.1021/acsnano.0c07993.

(21) Secor, E. B. Principles of Aerosol Jet Printing. *Flex. Print. Electron.* **2018**, *3* (3), 035002. https://doi.org/10.1088/2058-8585/aace28.

(22) Balderas, J. U.; Navarro, D.; Vargas, V.; Tellez-Cruz, M. M.; Carmona, S.; Falcony, C. Ultrasonic Spray Deposition as a New Route to Luminescent MOF Film Synthesis. *J. Lumin.* **2019**, *212*, 322–327. https://doi.org/10.1016/j.jlumin.2019.04.051.

(23) Arslan, H. K.; Shekhah, O.; Wohlgemuth, J.; Franzreb, M.; Fischer, R. A.; Wöll, C. High-Throughput Fabrication of Uniform and Homogenous MOF Coatings. *Adv. Funct. Mater.* **2011**, *21* (22), 4228–4231. https://doi.org/10.1002/adfm.201101592.

(24) Hurrle, S.; Friebe, S.; Wohlgemuth, J.; Wöll, C.; Caro, J.; Heinke, L. Sprayable, Large-Area Metal-Organic Framework Films and Membranes of Varying Thickness. *Chem. - Eur. J.* **2017**, *23* (10), 2294–2298. https://doi.org/10.1002/chem.201606056.

(25) Kim, D.-Y.; Joshi, B. N.; Lee, J.-G.; Lee, J.-H.; Lee, J. S.; Hwang, Y. K.; Chang, J.-S.; Al-Deyab, S.; Tan, J.-C.; Yoon, S. S. Supersonic Cold Spraying for Zeolitic Metal–Organic Framework Films. *Chem. Eng. J.* **2016**, *295*, 49–56. https://doi.org/10.1016/j.cej.2016.03.029.

(26) Carné-Sánchez, A.; Imaz, I.; Cano-Sarabia, M.; Maspoch, D. A Spray-Drying Strategy for Synthesis of Nanoscale Metal–Organic Frameworks and Their Assembly into Hollow Superstructures. *Nat. Chem.* **2013**, *5* (3), 203–211. https://doi.org/10.1038/nchem.1569.

(27) Garcia Marquez, A.; Horcajada, P.; Grosso, D.; Ferey, G.; Serre, C.; Sanchez, C.; Boissiere, C. Green Scalable Aerosol Synthesis of Porous Metal–Organic Frameworks. *Chem. Commun.* **2013**, *49* (37), 3848. https://doi.org/10.1039/c3cc39191d.

(28) Thommes, M.; Kaneko, K.; Neimark, A. V.; Olivier, J. P.; Rodriguez-Reinoso, F.; Rouquerol, J.; Sing, K. S. W. Physisorption of Gases, with Special Reference to the Evaluation of Surface Area and Pore Size Distribution (IUPAC Technical Report). *Pure Appl. Chem.* **2015**, *87* (9–10), 1051–1069. https://doi.org/10.1515/pac-2014-1117.

(29) Lin, R.-B.; Li, L.; Zhou, H.-L.; Wu, H.; He, C.; Li, S.; Krishna, R.; Li, J.; Zhou, W.; Chen, B. Molecular Sieving of Ethylene from Ethane Using a Rigid Metal–Organic Framework. *Nat. Mater.* **2018**, *17* (12), 1128–1133. https://doi.org/10.1038/s41563-018-0206-2.

(30) Shi, Y.; Liang, B.; Alsalme, A.; Lin, R.-B.; Chen, B. Mechanochemical Synthesis of an Ethylene Sieve UTSA-280. *J. Solid State Chem.* **2020**, *287*, 121321. https://doi.org/10.1016/j.jssc.2020.121321.

(31) Carbonell, C.; Imaz, I.; Maspoch, D. Single-Crystal Metal−Organic Framework Arrays. *J. Am. Chem. Soc.* **2011**, *133* (7), 2144–2147. https://doi.org/10.1021/ja2002428.

(32) Zhuang, J.-L.; Ar, D.; Yu, X.-J.; Liu, J.-X.; Terfort, A. Patterned Deposition of Metal-Organic Frameworks onto Plastic, Paper, and Textile Substrates by Inkjet Printing of a Precursor Solution. *Adv. Mater.* **2013**, *25* (33), 4631–4635. https://doi.org/10.1002/adma.201301626.

(33) Feng, J. Q.; Optomec, Inc. A Computational Study of Particle Deposition Patterns from a Circular Laminar Jet. *J. Appl. Fluid Mech.* **2017**, *10* (4), 1001–1012. https://doi.org/10.18869/acadpub.jafm.73.241.27233.

(34) Johannsmann, D. *The Quartz Crystal Microbalance in Soft Matter Research: Fundamentals and Modeling*, 1st ed. 2015.; Soft and Biological Matter; Springer International Publishing : Imprint: Springer: Cham, 2015. https://doi.org/10.1007/978-3-319-07836-6.

(35) Reviakine, I.; Johannsmann, D.; Richter, R. P. Hearing What You Cannot See and Visualizing What You Hear: Interpreting Quartz Crystal Microbalance Data from Solvated Interfaces. *Anal. Chem.* **2011**, *83* (23), 8838–8848. https://doi.org/10.1021/ac201778h.

(36) Sing, K. S. W. Reporting Physisorption Data for Gas/Solid Systems with Special Reference to the Determination of Surface Area and Porosity (Recommendations 1984). *Pure Appl. Chem.* **1985**, *57* (4), 603–619. https://doi.org/10.1351/pac198557040603.

(37) Feng, J. Q. Sessile Drop Deformations under an Impinging Jet. *Theor. Comput. Fluid Dyn.* **2015**, *29* (4), 277–290. https://doi.org/10.1007/s00162-015-0353-x.

(38) Tafoya, R. R.; Secor, E. B. Understanding Effects of Printhead Geometry in Aerosol Jet Printing. *Flex. Print. Electron.* **2020**, *5* (3), 035004. https://doi.org/10.1088/2058-8585/aba2bb.

(39) Rammohan, A.; Dwivedi, P. K.; Martinez-Duarte, R.; Katepalli, H.; Madou, M. J.; Sharma, A. One-Step Maskless Grayscale Lithography for the Fabrication of 3-Dimensional Structures in SU-8. *Sens. Actuators B Chem.* **2011**, *153* (1), 125–134. https://doi.org/10.1016/j.snb.2010.10.021.

(40) Wesch, A.; Dahmen, N.; Ebert, K. H. Measuring the Static Dielectric Constants of Pure Carbon Dioxide and Carbon Dioxide Mixed with Ethanol and Toluene at Elevated Pressures. *Berichte Bunsenges. Für Phys. Chem.* **1996**, *100* (8), 1368–1371. https://doi.org/10.1002/bbpc.19961000816.

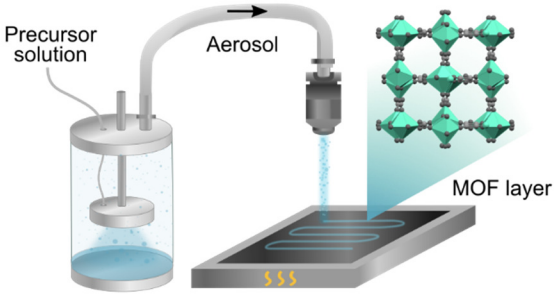


For Table of Contents Only